Optical Coherence Microscopy. A Technology for Rapid, in Vivo, Non-Destructive Visualization of Plants and Plant Cells[1][w]

James W. Hettinger, Matthew de la Peña Mattozzi, Whittier R. Myers[2], Mary E. Williams, Aaron Reeves, Ronald L. Parsons, Richard C. Haskell, Daniel C. Petersen, Ruye Wang, and June I. Medford*

Department of Biology, Colorado State University, Fort Collins, Colorado 80523–1878 (J.W.H., A.R., R.L.P., J.I.M.); and Departments of Biology (M.d.l.P.M., M.E.W.), Physics (W.R.M., R.C.H., D.C.P.), and Engineering (R.W.), Harvey Mudd College, Claremont, California 91711

We describe the development and utilization of a new imaging technology for plant biology, optical coherence microscopy (OCM), which allows true in vivo visualization of plants and plant cells. This novel technology allows the direct, in situ (e.g. plants in soil), three-dimensional visualization of cells and events in shoot tissues without causing damage. With OCM we can image cells or groups of cells that are up to 1 mm deep in living tissues, resolving structures less than 5 μm in size, with a typical collection time of 5 to 6 min. OCM measures the inherent light-scattering properties of biological tissues and cells. These optical properties vary and provide endogenous developmental markers. Singly scattered photons from small (e.g. $5 \times 5 \times 10$ μm) volume elements (voxels) are collected, assembled, and quantitatively false-colored to form a three-dimensional image. These images can be cropped or sliced in any plane. Adjusting the colors and opacities assigned to voxels allows us to enhance different features within the tissues and cells. We show that light-scattering properties are the greatest in regions of the Arabidopsis shoot undergoing developmental processes. In large cells, high light scattering is produced from nuclei, intermediate light scatter is produced from cytoplasm, and little if any light scattering originates from the vacuole and cell wall. OCM allows the rapid, repetitive, non-destructive collection of quantitative data about inherent properties of cells, so it provides a means of continuously monitoring plants and plant cells during development and in response to exogenous stimuli.

Studies in plant physiology and development characteristically follow changes in space and time that occur as part of normal plant activity or in response to exogenous stimuli. Typical studies require the destruction and analysis of a plant or a tissue sample, followed by the collection and analysis of a second distinct plant or sample. Thus, biological responses or changes are inferred by comparing different plants or samples. Such approaches have been used for centuries and have produced a great deal of knowledge. However, when scientists are able to non-destructively follow biological changes, important concepts and insights have emerged. For example, critical genes involved in programmed cell death were found in *Caenorhabditis elegans* partially because the developing nematode is nearly transparent, allowing the fate of each cell to be followed in vivo by light microscopy (Gilbert, 1998). Similarly, an elegant fate map for Arabidopsis roots was constructed because the relatively transparent roots allow changes in individual plants to be followed continuously (Dolan et al., 1993). This study led to new discoveries such as the presence of downward communication between mature root cells and the root apical meristem and short-range control of differentiation signals (van den Berg et al., 1997a, 1997b).

Except for the relatively transparent Arabidopsis root, plants provide a challenge for in vivo analyses. For example, plant shoots are highly pigmented and many key processes take place in cells and tissues that are deeply buried. Technologies that allow a limited type of in vivo imaging of plants have been developed. For example, magnetic resonance imaging (MRI) allows imaging of plants (Faust et al., 1997). However, image collection requires a long time period, and the relatively low resolution generally limits its use to large morphological features such as those in fruits and seeds (Faust et al., 1997). Confocal microscopy allows imaging of transgenic plants containing green fluorescent protein (GFP) or fixed plants stained with propidium iodide (Running et al., 1995; Haseloff, 1999). Imaging with GFP, however, is limited to relatively shallow depths of 60 to 80 μm (Haseloff, 1999). Also, GFP imaging appears to involve the production of free radicals, which are potentially damaging to the plant (Haseloff, 1999). Because of its shallow penetration depths, confocal imaging of the shoot apex typically involves the re-

[1] This work was supported by the National Science Foundation (grant no. DBI–9612240 to R.C.H., D.C.P., R.W., M.E.W., and Scott Fraser [California Institute of Technology]).

[2] Present address: Department of Physics, 366 LeConte Hall, University of California, Berkeley, CA 94720–7300.

[w] The on-line version of this article contains Web-only data. This version is available at www.plantphysiol.org.

* Corresponding author; e-mail medford@lamar.colostate.edu; fax 970–491–0649.

moval of overlying leaves (Running et al., 1995; Haseloff, 1999). Furthermore, because confocal microscopy and GFP imaging often require a fluorescence excitation light source, endogenous autofluorescence from plant pigments and cell walls can interfere with imaging.

We have developed and used a new imaging technology for plants, optical coherence microscopy (OCM). Plant cells and intact plants are imaged directly (e.g. in soil) without any type of stain, pretreatment, or transgene insertion. The technology uses the natural penetration of light into living tissues and the back-scattering of photons from inherent cellular components (Fujimoto et al., 1998). Back-scattered photons are collected, measured, and used to assemble an image. Therefore, we have developed a technology that allows us to rapidly, continuously, and noninvasively follow micrometer-size changes within plant tissues.

RESULTS

OCM

The remarkable achievement of OCM is the ability to image cells located up to 1 mm deep in tissue. Overlying tissue that is highly scattering obscures these deeper structures when using any other type of optical microscopy. Figure 1A illustrates this point. An image of deep target cells can be formed with photons that illuminate the cells, scatter once from the cells, and are subsequently collected by a lens. However, most photons collected by the lens will have been scattered once or multiple times from the overlying tissue, probably never encountering the cells of interest. These photons carry no information about the target cells. OCM preferentially selects those photons that have been scattered once from the target cells by requiring that all photons used to form an image have traveled a specified total path length in the tissue. For example, in Figure 1A (left), the total path length required could be the distance from the air-tissue interface to the target cells and back up to the tissue-air interface, where photons are collected by the lens. Most photons scattered by the overlying tissue will not have this particular total path length and will be excluded from the image formation process (Fig. 1A, right). This exclusion is not absolute: some photons that are multiply scattered from overlying tissue will satisfy the path length requirement, and these photons ultimately place a limit on the depth to which OCM is effective.

OCM imaging involves two steps, the collection of back-scattered light from plants, and then the visualization of the data sets as three-dimensional images. The optical principles behind this type of imaging have been reviewed by Masters (1999) and Fercher (1996). Our instrument is similar to that described by Izatt (1996). A more detailed description of the instrument is provided by Hoeling et al. (2000).

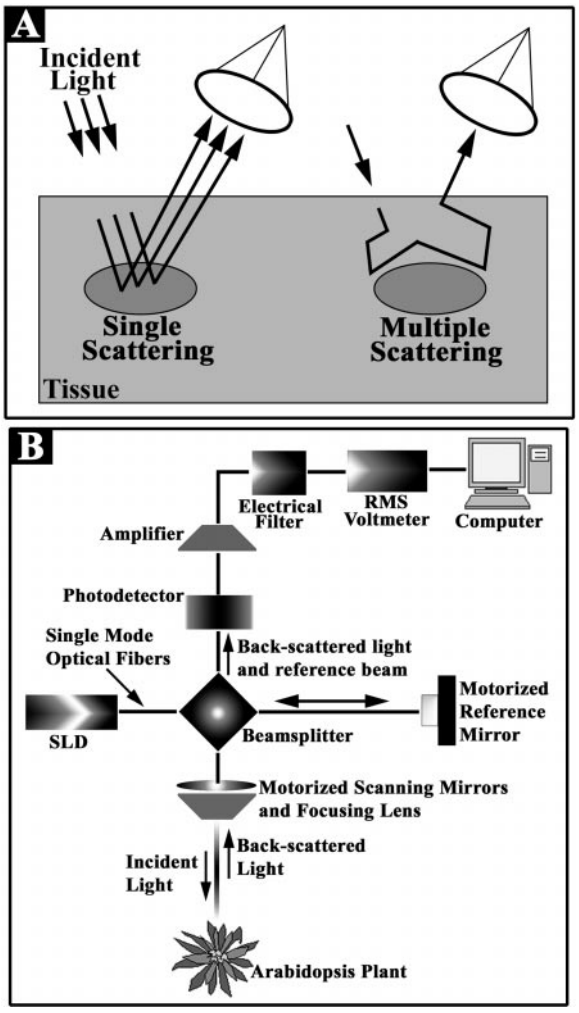

Figure 1. Optical coherence microscope: fundamental principle and schematic. A, In forming an image of deep target cells, OCM preferentially selects photons that are singly scattered from the target cells (left) and rejects photons that are scattered from overlying tissue (right). B, Near-infrared light (850 nm) is emitted by an SLD and travels along a single-mode optical fiber to the beamsplitter of a Michelson interferometer. Roughly 50% of the light travels along an optical fiber to a reference mirror whose position is controlled by a computer. The other 50% of the light travels along an optical fiber to the sample and is focused to a 5-μm diameter spot in the plant tissue. A pair of rotating mirrors moves the focused spot across the *x-y* plane. To move the focused spot deeper into the tissue, motorized actuators translate the lens toward the plant. Photons traveling the same path length in the sample and reference arms combine to form interference fringes on the photodetector at the output of the Michelson interferometer. The amplitude of the fringes is measured electronically and stored in the computer as the beam is scanned through the sample volume. Fringe amplitude is proportional to the square root of the scattering coefficient of the sample volume element under examination.

A schematic of the OCM instrument we used is shown in Figure 1B. Near-infrared light at 850 nm (for good penetration in tissue) was provided by a very low intensity (300-μW) superluminescent diode (SLD) so that there was no damage to the plant or

plant cells. The light beam travels along single-mode optical fibers. The light is split (50/50), with half going along the sample arm to the plant and half going along the reference arm to a mirror. In the sample arm the light beam is focused to a diameter of approximately 5 μm. The coherence length of the SLD is 10 μm, so the resolution volume probed at any particular time is 5 μm in diameter by 10 μm long. Rotating mirrors are used to move the light beam in the transverse directions (x and y) at a specified depth (z plane). A typical scan will collect back-scattered light from 100 voxels along both the x and y directions (for 10,000 voxels in a single z plane).

The distance the beam moves between voxels is adjustable, which affects both the sampling interval and the size of the image. After each scan of a z plane, the focusing lens is stepped down in depth and another z plane is scanned. Light back-scattered from each voxel returns via the sample arm optical fiber to the beamsplitter, where it recombines with light returning from the reference mirror of a Michelson interferometer (Fig. 1B). If the path lengths in the reference and sample arms are the same to within a coherence length of the SLD (approximately 10 μm), interference fringes will be recorded by the photodetector. The amplitude of the fringes is recorded and stored in computer memory as a three-dimensional data set. The fringe amplitude is proportional to the square root of the intensity back-scattered from each tissue voxel, so the OCM image is a quantitative measure of the back-scattering property of the tissue.

Light scattered by tissue overlying the cells of interest may also return via the sample arm optical fiber. However, most of this light will have traveled a different total path length and will not contribute to interference fringes at the photodetector. The OCM records the amplitude of the interference fringes only, so photons scattered by overlying tissue are effectively rejected and do not contribute to the OCM image.

OCM Images of Plants

OCM images can be obtained of plants growing in soil without any type of treatment, staining, or transgenic production. Our early OCM studies indicated that trichomes back-scattered an inordinately large amount of light, which masks the underlying light scattering of plant tissues and organs. This observation is corroborated by a previous study showing that trichomes greatly scatter light (Gausman, 1977). To avoid the problematic light scattering from trichomes, we used plants with a trichome deficiency (*glabrous-1*, *gl-1*) as our standard genetic background.

Figure 2A shows an OCM image of an Arabidopsis shoot. This image is derived from back-scattered light from 1 million voxels (100 voxels in each dimension) that are spaced 7.5 $\times$ 7.5 $\times$ 5 μm ($x \times y \times z$)

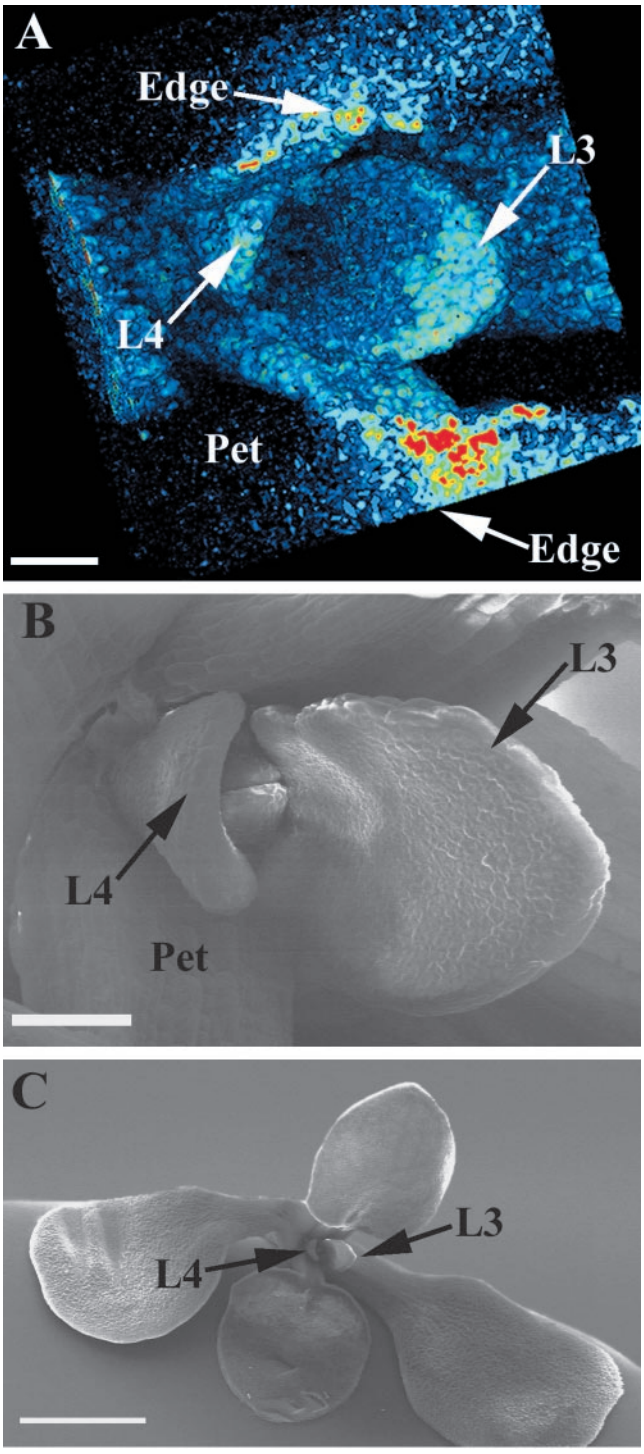

Figure 2. OCM and SEM images of a 9-d-old Arabidopsis plant. A, Three-dimensional OCM image of an Arabidopsis shoot. The image is 750 μm in x and y, and 500 μm in depth (into the page, z). Leaves 3 and 4 and the petiole of an older leaf are indicated. This image has been rotated slightly to align better with the SEM images. Edges of the scanned volume are indicated with arrows. B, Scanning electron micrograph of the same plant as in A at a magnification close to that of the OCM. C, Scanning electron micrograph at a lower magnification showing the entire shoot. L3 and L4, Leaf primordia 3 and 4; Pet, petiole. Scale bars in A and B = 100 μm and C = 1 mm.

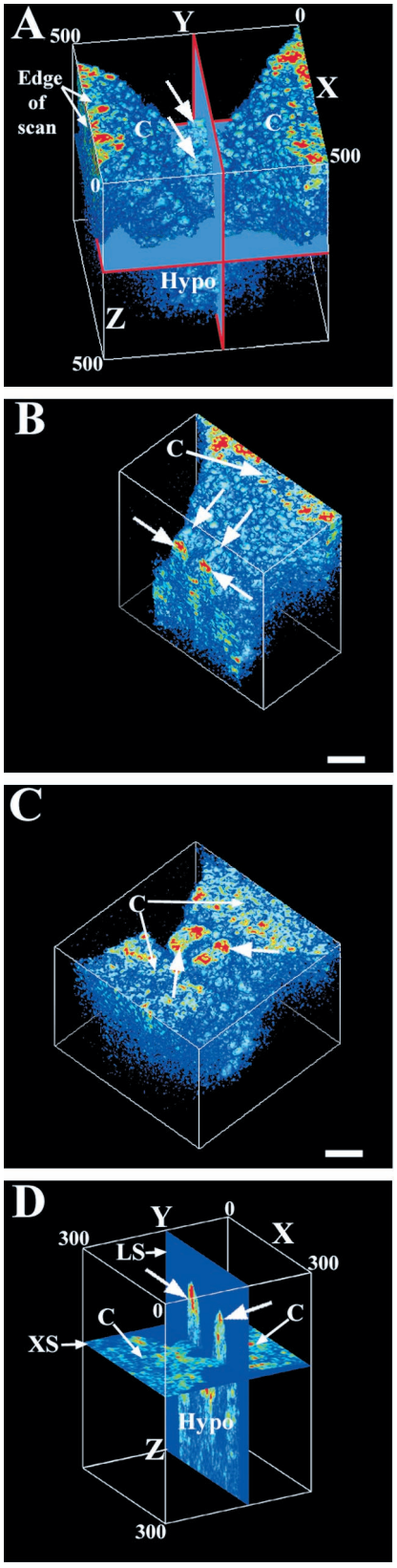

Figure 3. OCM three-dimensional data sets allow noninvasive cropping and slicing of images. A, OCM image (500-μm)^3 of an 8-d-old Arabidopsis shoot. The voxels are assembled to produce a three-dimensional volume that can be rotated, cropped, or sliced in any plane. Solid panels were inserted in the *y* and *z* planes to demonstrate the three-dimensional nature of the image. White lines define the edges of the scanned volume. The letters and numbers (in μm) at the edges of the box represent the sizes and dimensions. B, *y* axis crop. Voxels with *y* values greater than 225 μm were removed to reveal the interior of the leaf primordia. C, *z* axis crop. The same data set was cropped to remove voxels with *z* values less than 135 μm, revealing a cross-sectional view of the leaf primordia. D, OCM images can also be viewed as slices. An OCM image of a different and slightly older plant is shown as two intersecting slices, resembling conventional longitudinal and cross-sectional slices. Arrows point to leaf primordia in all panels. C, Cotyledon petiole; Hypo, hypocotyl; LS, longitudinal slice; XS, cross-sectional slice. Scale bars in B and C = 50 μm.

apart. The OCM data shown in Figure 2A are displayed so that voxels are opaque (high α-parameter in AVS Express software, see below). The result of the high opacity is a surface-rendered image that resembles an image from scanning electron microscopy (SEM). The sample orientation and surface rendering of this low-resolution OCM image effectively hid leaf primordium 5 (see below). To test the accuracy of the OCM image, within minutes of collecting the image, the plant was removed from the soil, fixed, and subsequently examined with SEM. Figures 2B and 2C show SEMs of the same plant as in Figure 2A. The SEM in Figure 2B shows leaf primordia 3 and 4, which are readily visible in Figure 2A, while Figure 2C shows a low-magnification view of the entire shoot for orientation purposes. The OCM image closely resembles that obtained through traditional SEM. However, the OCM images were obtained from living plants growing in soil and took 5.5 min to acquire, whereas SEM required killing the plant and multiple preparation steps over several days. In addition to rapid, in vivo imaging, OCM provides information significantly beyond that of SEMs. As described below, OCM provides quantitative data about inherent properties of cells and allows the interior structures and tissues to be visualized directly and non-destructively.

OCM Images Are Assembled to Produce True Three-Dimensional Volumes

Figure 3A shows a 500- $\times$ 500- $\times$ 500-μm OCM image of an 8-d-old Arabidopsis shoot. The cotyledon petioles are oriented parallel to the *y* axis, while leaf primordia 1 and 2 (arrows) are opposite each other along the *x* axis. Gray panels were inserted into Figure 3A to emphasize the three-dimensional nature of the data. The voxels are false-colored so that voxels with the lowest values (i.e. the lowest amount of back-scattered photons) are blue, voxels with intermediate values are greenish-yellow, and voxels with the highest values are red. Figure 3, B and C, show the data set in Figure 3A cropped in the *y* and *z* planes, respectively. In Figure 3B, the data set shown in Figure 3A was cropped to eliminate all voxels with

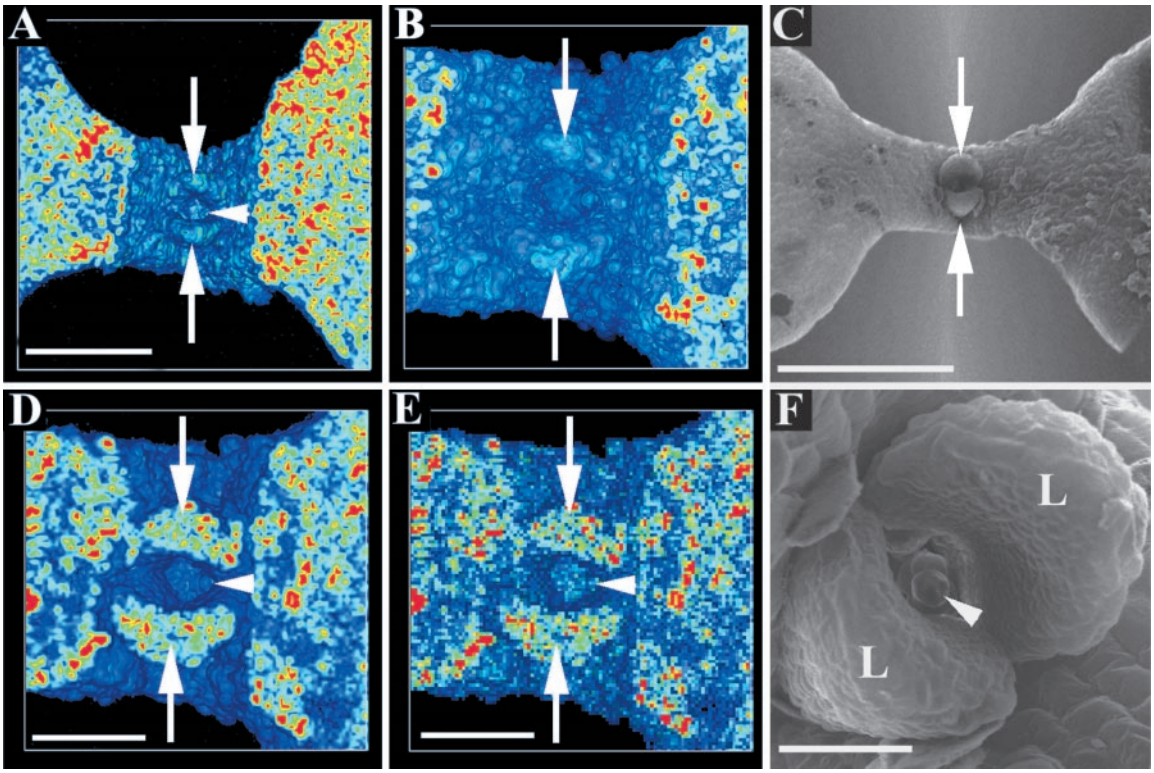

Figure 4. Effects of voxel spacing and smoothing algorithm on visualization of OCM data. All panels show the same 7-d-old Arabidopsis plant. All panels (except F) are oriented with the cotyledons or cotyledon petioles at the panel sides. A, OCM image produced with voxels spaced 7 μm apart. Arrows indicate leaf primordia; arrowhead indicates stipules. B, OCM image produced with voxels spaced 3 μm apart. C, SEM image of the plant shown in A, B, D, and E. The same data set as shown in B was cropped to remove some of the voxels including those of the outermost surface of the leaf primordia. D, Image smoothed using AVS trilinear algorithm. E, Image generated without the smoothing algorithm. F, Higher magnification SEM in which stipules can be seen (arrowhead). Scale bars in A = 250 μm; B, D, and E = 100 μm; C = 500 μm; and F = 50 μm.

y coordinates greater than 225 μm, effectively "cutting into" the developing leaf primordia and hypocotyl. In Figure 3C, the data set was cropped to remove all voxels with z coordinates less than 135 μm, effectively producing a "cross-sectional" view of the leaf primordia and cotyledon petioles. In cross-section, the highest light-scattering regions are seen at the lateral edges of the leaf primordia in a position consistent with the developing leaf blade (McHale, 1993; Tsuge et al., 1996). To further demonstrate the three-dimensional nature of the OCM data, we have assembled a video showing this data set cropped in each plane and rotated (compare with http://www.colostate.edu/Depts/Biology/OCM and http://www.plantphysiol.org). Figure 3D shows that OCM data can be visualized in any plane as voxel-thick volumes or slices. In Figure 3D, an OCM image of a different (slightly older) Arabidopsis shoot is shown as two intersecting, two-dimensional slices.

Visualization of OCM Data Sets

All of the three-dimensional data sets were imaged using AVS Express.

Effects of Voxel Sampling Density

The voxel probed by the OCM at any particular time is a cylinder approximately 5 μm in diameter by 10 μm in depth. However, by collecting light from voxels spaced more closely than 5 μm, finer detail can normally be seen, particularly when there is a large difference in scattering properties between neighboring voxels. (A similar strategy was recently reported to improve image quality in ophthalmological studies: Gurses-Ozden et al., 1999.) Decreasing voxel density allows a larger area to be scanned, but results in an image with less detail (e.g. Fig. 2A). To account for the effect of voxel sampling density, we typically perform two scans of a sample: a large-area scan with less definition and a small-area scan with more definition. Figure 4, A and B, shows two images of the same Arabidopsis plant taken within minutes of each other but with a voxel spacing of $7 \times 7 \times 5$ μm or $3 \times 3 \times 5$ μm, respectively. The image shown in Figure 4A was collected with lower voxel density, so it includes a wider area but has less definition than the image shown in Figure 4B. The image collected with higher voxel density provides finer detail about

the structure of the plant and its inherent light-scattering properties. For comparison, SEMs of the same plant are shown in Figure 4, C and F.

Boundary Effect

The boundary of the plant tissue is typically false-colored blue in our OCM images. At the micron level, the edge of a plant is irregular and never precisely fills a voxel. Therefore, the voxels at the air-tissue interface, or boundary voxels, normally have low values, as only a portion of their volume represents tissue. When the boundary voxels are not included in the image, the higher light-scattering regions within the tissue are more apparent. Boundary voxels can be excluded in two ways. In the image shown in Figure 4A, the scan begins within the tissue of the cotyledons, so the air-tissue boundary is excluded and the underlying light scattering of the cotyledons is evident. Similarly, the boundary voxels can be removed by cropping the image, which reveals the light scattering of the underlying tissue. For example, compare Figure 4B, in which the leaf primordia appear blue because of the boundary voxels, with Figure 4, D and E, in which the same data set has been cropped to remove some of the voxels, including those at the air-tissue interface.

Interpolation

We use two different methods to project our three-dimensional data sets onto a two-dimensional viewing screen. All OCM images shown to this point have been constructed using the trilinear algorithm, which interpolates between voxels in the AVS Express software. When displayed using the trilinear algorithm, OCM images show morphological features resembling those seen with direct visualization or SEM. In contrast, images may also be rendered using a nearest-neighbor algorithm (point algorithm). When the point algorithm is used, each display element of any plane in the three-dimensional volume is based on the value of a single voxel, rather than an interpolation of several voxel values. We routinely examine our OCM images with both the point algorithm and the trilinear algorithm. Figure 4, D and E, show the same data set displayed with the trilinear algorithm or with the point algorithm. With the point algorithm, individual voxels are seen and the overall image appears pixelated (Fig. 4E). With the trilinear algorithm, the image appears less jagged or smoothed. Because of the better morphological appearance displayed with the trilinear algorithm, we routinely employed it for most images.

Colormaps and α-Settings

The software employed to visualize the OCM data allows a wide range of options for data display. These options, used to control the way in which data are false-colored, are valuable as they allow us to visualize different features and produce see-through images. Figure 5, A through D, display a portion of the same data set shown in Figure 4, B, D, and E, but cropped and rotated so that only one leaf primordium is displayed. Because our system crops (or slices) in voxel volume increments, and organs in the shoot apex are at times touching each other, we cannot cleanly isolate a leaf primordium from surrounding tissues in images of this plant (Fig. 5A, arrowhead). Figure 5A shows the leaf primordium viewed with the same settings as used in Figures 2 through 4, in which the blue boundary voxels are rendered opaque, resulting in a surface view. The slightly concave adaxial and convex abaxial surfaces of the primordium are evident. The plant's prominent stipules (Fig. 4F) have been sliced into and appear as highly scattering structures in the OCM image (marked "S" in Fig. 5A).

We adjusted the color assigned to voxels of various values, or the colormap, so that voxels with low values corresponding to background (electrical) noise are transparent and appear black. Voxels with values above the noise level are assigned colors ranging from blue (low values) to red (high values) using a linear scale. The voxel values are proportional to the square root of the light back-scattering coefficient (Hoeling et al., 2000). At the bottom of each panel we have placed the exact colormap used to produce each image. In Figure 5A, the colormap indicates that the features within the stipules that are false-colored red are approximately $(240/15)^2$, or 256, times more highly light scattering than the blue boundary voxels at the surface of the primordium.

We can adjust the apparent voxel opacity (α-parameter) independently of the colormap to reveal the internal structure of the tissue. In Figure 5A, the voxels are opaque, and only the blue boundary voxels of the leaf primordium are evident. Figures 5B and 5C show the effects of reducing the opacity (α-parameter). By reducing the tissue opacity, a high light-scattering region at the distal region of the leaf primordium is seen (indicated by an arrow in Fig. 5B).

By adjusting the colormap, without altering the opacity, we can enhance the appearance of voxels of intermediate light-scattering values. In Figure 5D the colormap is compressed as indicated and an intermediate light-scattering pattern, false-colored an orange-yellow, is seen to form a horseshoe-shaped pattern within the leaf primordium. However, by compressing the colormap, the quantitative differences between red and blue are reduced. In Figure 5D, voxels colored red are at least $(105/15)^2$, or 49-fold, more light scattering than those colored blue. The three-dimensional nature of this horseshoe-shaped pattern is better demonstrated when the leaf primordium's image is rotated (see http://www.plantphysiol.org). Furthermore, when the leaf pri-

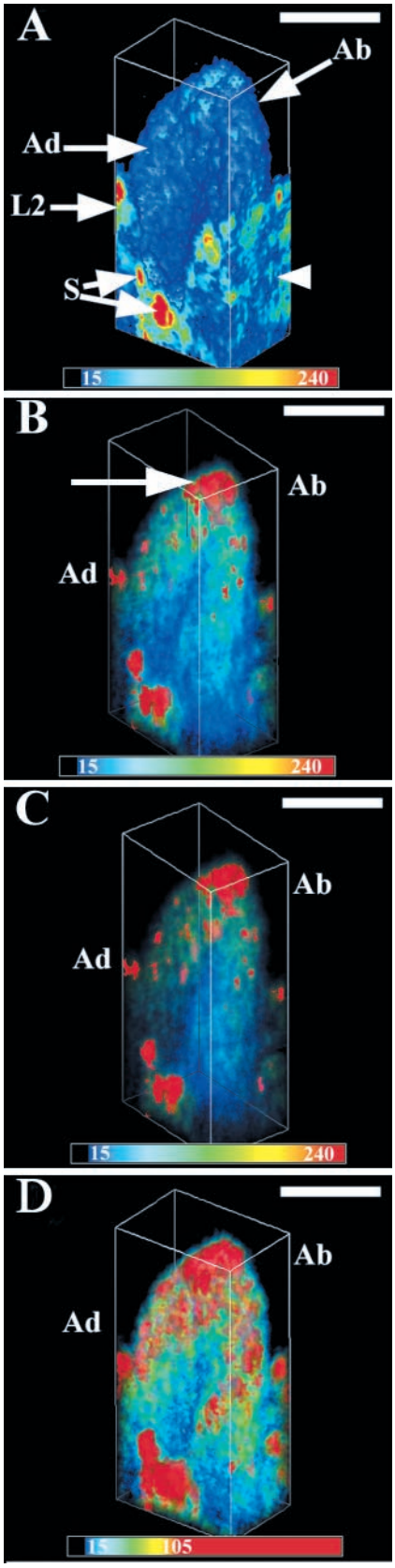

Figure 5. Adjusting the α-parameter and colormap allows different aspects of the data to be emphasized. The same data set seen in Figure 4B was cropped to display only one leaf primordium. The exact color map used to produce the image is seen at the base of each panel. Voxels of higher light scattering are colored red. A, Images displayed with a high opacity show outside features like those of an SEM. Stipules (indicated by arrows) are highly light scattering. Arrowhead indicates residual cotyledon tissue. B, The opacity with which voxels are displayed can be reduced by adjusting the α-parameter, allowing underlying light-scattering patterns to be seen. Arrow indicates a highly scattering region at the distal end of the leaf primordium. C, Lowering the α-parameter more renders an image that is nearly completely transparent. D, Image produced using the same α-factor as in C, but in which the color map has been compressed, rendering voxels of intermediate value in reds and yellows. Ab, Abaxial surface; Ad, adaxial surface; L2, a portion of leaf primordium 2 that was not cropped from this image; S, stipules. Scale bars in A through D = 100 μm. A dynamic presentation of the effects of adjusting the α-parameter and color map and a rotation of the leaf primordium's image can be found at http://www.plantphysiol.org.

mordium is rotated, the high light scattering at the distal-most tip appears more prevalent toward the adaxial surface of the developing primordium.

Visualization of Cells/OCM Resolution

In the images shown in Figures 2 through 5, individual cells are not distinctly resolved. In Arabidopsis meristems and young leaf primordia, cells are typically 5 to 10 μm in size (Medford et al., 1992), which is near the size of the volume element probed by our OCM (Hoeling et al., 2000). To determine if OCM can resolve individual cells and subcellular features, we examined larger cells in planta and in culture.

Figure 6A shows an in planta image of maize leaf cells from a 14-d-old maize plant. The long axis of the leaf runs from the left to right, parallel to the long axes of the cells. Highly light-scattering regions are apparent at the periphery of the cells. As maize leaf cells are highly vacuolated, this region encompasses both the cytoplasm and the cell wall. To identify which cellular features are the cause of the light scattering, we examined large, vacuolated cells from an aneuploid Arabidopsis suspension culture line (Davis and Ausubel, 1989). Figures 6B and 6C show the optical coherence and light microscope images, respectively, of a cluster of suspension-cultured cells. The prominent nuclei (arrows) and large vacuoles typical of these cells are evident in the bright-field light microscope image (Fig. 6C). In the OCM image, the nuclei (arrows) are highly scattering and therefore false-colored red (Fig. 6B). The cytoplasm, which is closely pressed against cell walls, produces less light scatter, and these intermediate scattering values are false-colored yellow-green. Figure 6, D through F, show a different cluster of cells that have a sea horse shape. In the dark-field light microscope image, the cytoplasmic membrane of the second cell from the bottom has retracted from the cell wall and appears as a wavy protoplast (Fig. 6E, arrowhead). In the

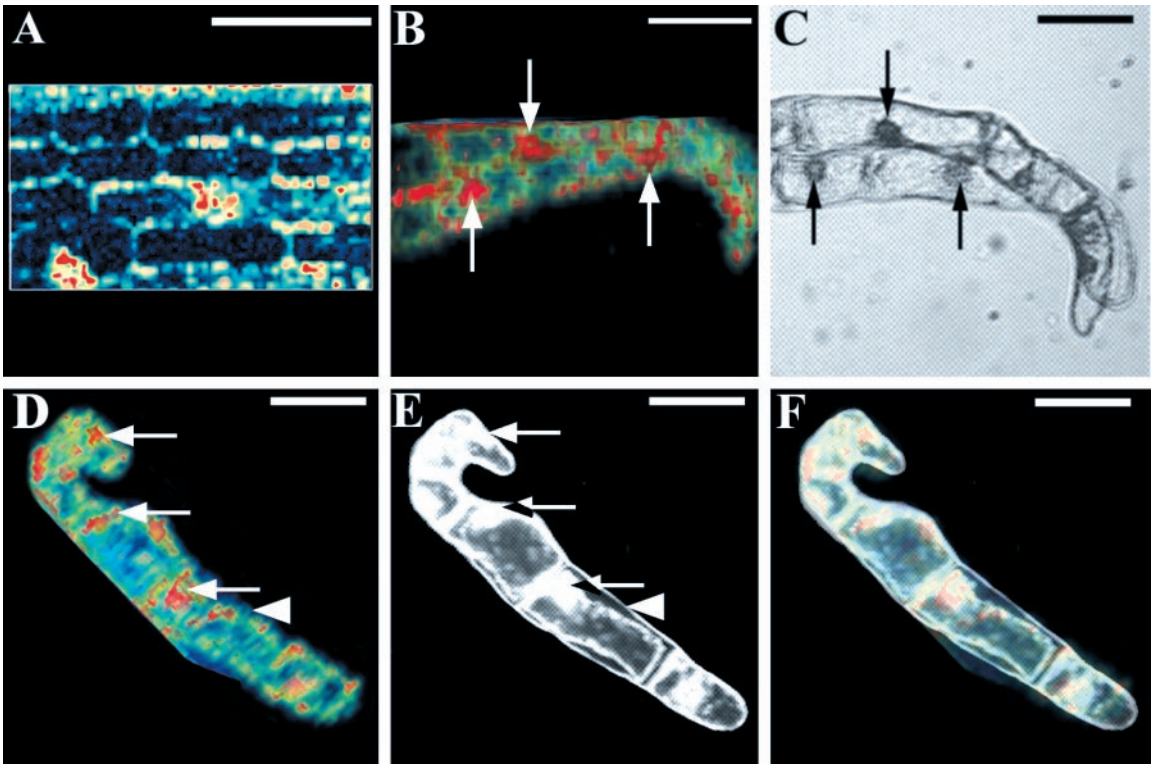

Figure 6. OCM images of cells. A, OCM image of epidermal cells in maize leaf. Light-scattering region corresponds to the region of the cell wall and cytoplasm. B through F, Arabidopsis aneuploid suspension-cultured cells. B, OCM image of a clump of cells with arrows indicating nuclei. C, Light micrograph of same cells. D, OCM image of another group of suspension-cultured cells. Arrows point to nuclei. Arrowhead points to wavy protoplast surface. E, Dark-field light micrograph of the same cells seen in D. In the second cell from the right, the cytoplasm has pulled away from the cell wall. Arrowhead points to the cell wall. F, Images from D and E superimposed. The light-scattering regions correspond to the nuclei and cytoplasm, but not the cell walls. Scale bars in A through C = 50 μm and D through F = 25 μm.

OCM image (Fig. 6D), the light-scattering region follows the wavy curve of the protoplast, rather than the straight line of the cell wall. This feature is particularly apparent when the OCM and light micrograph images are superimposed (Fig. 6F). The images shown in Figure 6 indicate that in plant cells, light is predominantly back-scattered from the nucleus and the cytoplasm rather than from the cell walls.

In Planta OCM Images Compared with Sections

Figure 7 shows a comparison of OCM images with thin histological sections. All histological sections are 1 μm and all OCM sections are 10 μm thick. Figures 7A and 7B show a histological cross-section and a slice of an OCM image through the young leaves of a 7-d-old Arabidopsis plant. The light micrograph shows densely cytoplasmic cells in leaves 1 and 2 (Fig. 7A). In the OCM image, the densely cytoplasmic cells produce a high light-scattering pattern (red). Overlaying these two images demonstrates that the OCM images faithfully represent the plant morphology (Fig. 7C).

A comparison of slices from farther down the axis of the same plant, where the developing organs are covered by overlying tissue, is shown in Figure 7, D through F. Leaf primordia 3 and 4 are initiated opposite to one another and develop with the adaxial sides very close to each other (Fig. 7D; Medford et al., 1992). These organs can be seen in the center of the OCM image. A prominent stipule can be seen behind the abaxial side of leaf primordium 3 in both the histological and OCM slices (Fig. 7, D and E). Again, overlaying these images confirms the fidelity of the OCM images, although in this case the OCM section is slightly tilted relative to the histological section.

Figures 7G and 7H show a comparison of slices through the shoot apical meristem from another 11-d-old Arabidopsis plant. By the time it was imaged and fixed for sectioning, this plant had initiated five leaves and the youngest leaf primordium was still somewhat radial (Fig. 7G). Figure 7H shows that developing leaf primordia and the shoot apical meristems are highly light scattering (red), but the highly light-scattering regions are not uniform throughout. In leaf primordia, the high light-scattering region corresponds to the areas with densely cytoplasmic cells (Fig. 7, G–I). In the apical meristem the high light scattering is also not uniform, but in this case is more prevalent on the side away from leaf primor-

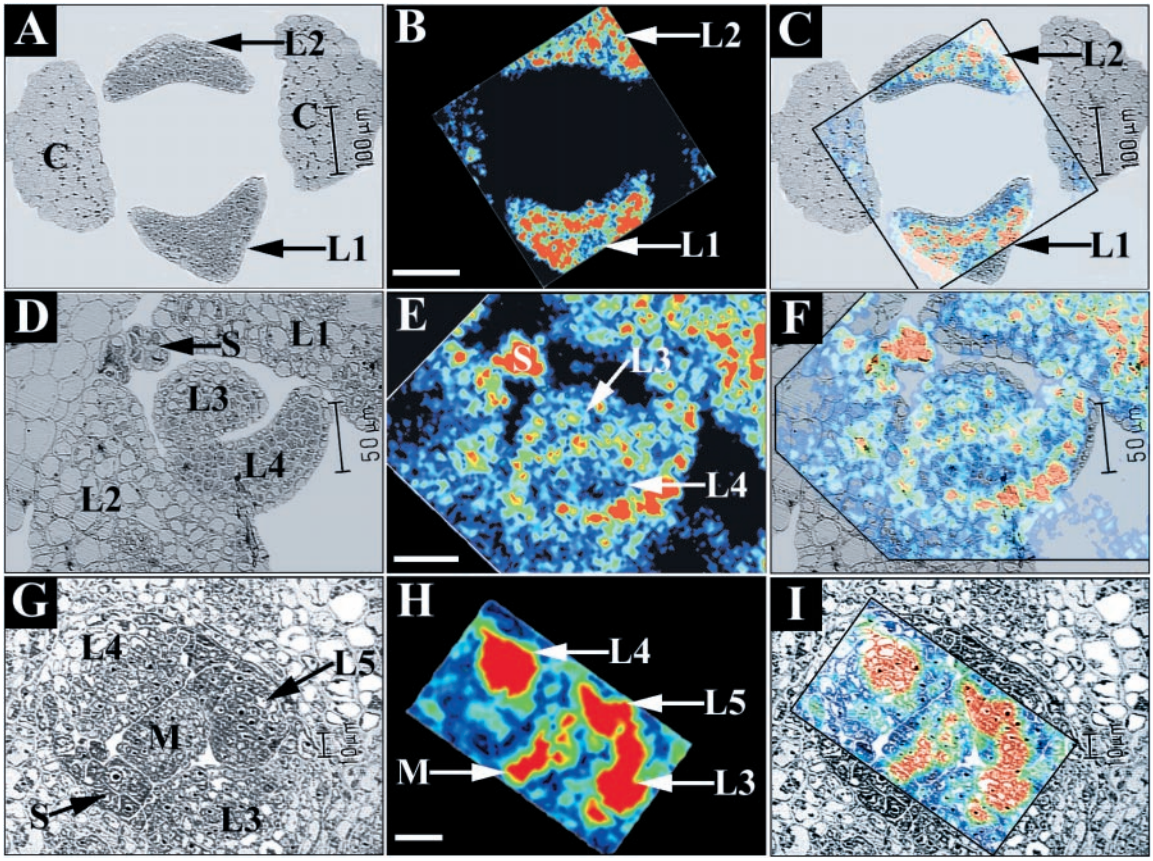

Figure 7. Comparisons of OCM slices and histological sections demonstrate that OCM imaging faithfully reproduces plant morphology. All histological sections are 1 μm thick and all OCM sections are in the smallest voxel volume increment, in this case 10 μm thick. A, Plastic cross-section through leaves 1 and 2 of Arabidopsis plant. B, OCM slice from approximately the same plane as the plastic section of the same plant. C, Images from A and B superimposed to show the close match between the OCM slices and histological sections. D through F, Images as in A through C, but approximately 200 μm into the shoot apex, showing leaf primordia 3 and 4. D, Plastic section. E, OCM image. F, Superimposed images. G through I, As in A through C but a different Arabidopsis plant, showing the shoot apical meristem and leaf primordia 3, 4, and 5. G, Plastic section. H, OCM image. I, Superimposed images. Scale bars in A through C = 100 μm, D through F = 50 μm, G and I = 10 μm, and H = 20 μm.

dium 5 (Fig. 7I). Although the light-scatter patterns were highly reproducible with scans 6 min apart, our preliminary studies show that light-scattering patterns in developing organs and the shoot apical meristem are dynamic, at times changing over periods as short as 1 to 2 h (J. Hettinger, A. Reeves, R.L. Parsons, M.E. Williams, R.C. Haskell, D.C. Petersen, R. Wang, and J.I. Medford, unpublished data).

OCM Analysis of the *shootmeristemless-1* (*stm-1*) Mutant

To confirm that the highly light-scattering regions shown in Figure 7 correspond to the shoot apical meristem and developing leaf primordia, we examined OCM images of the *stm-1* mutant. The severe *stm-1* allele encodes a mutated homeodomain protein preventing formation of the apical meristem (Barton and Poethig, 1993; Long et al., 1996). Figures 8A and 8B show OCM and SEM images of the same *stm-1* mutant. In the central part of the shoot, there are no highly light-scattering regions and no images of organs in the OCM image, confirming that the highly light-scattering regions seen in wild-type plants correspond to the shoot apical meristem and leaf primordia.

DISCUSSION

Examining changes in organisms, tissues, and cells during development and in response to exogenous factors is an integral part of biology. Often, the organism or sample under study must be destroyed to obtain the desired information. The OCM imaging technology we describe offers a powerful new approach with which to examine living organisms noninvasively and over time. The strong correlation of the OCM and SEM images (Figs. 2–4 and 8) and the ability to superimpose light micrographs and OCM images of cells and plant sections (Figs. 6 and 7)

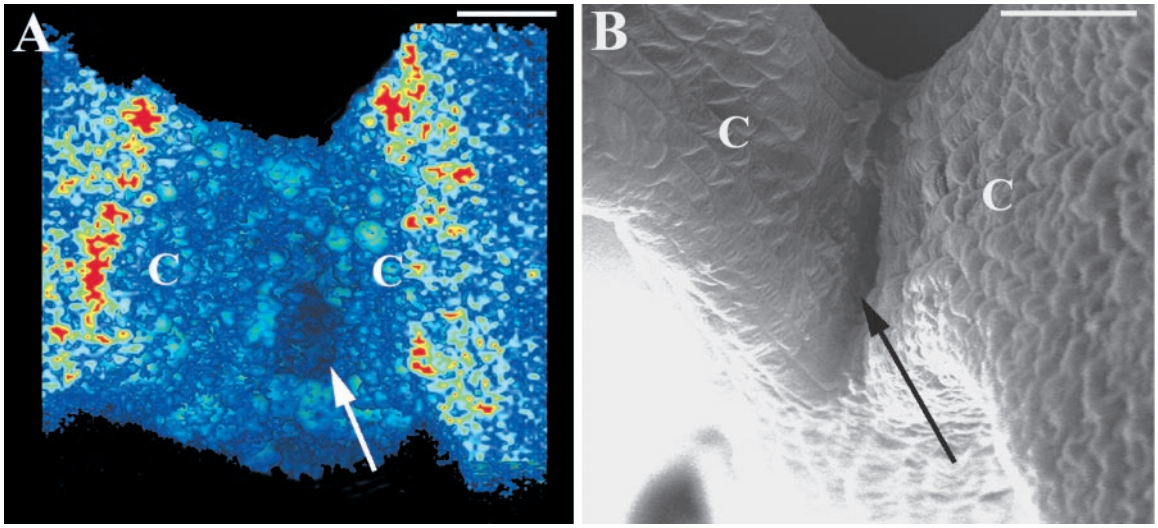

Figure 8. OCM and SEM images of *stm-1* mutant. A, An OCM image of the *stm-1* mutant does not show the highly light-scattering regions corresponding to the shoot apical meristem and leaf primordia. The arrow indicates the position at which the shoot apical meristem would be in a wild-type plant. B, An SEM of the same plant as in A. C, Cotyledon. Scale bars in A and B = 100 μm.

indicates that OCM provides consistent and realistic images of plant cells and intact plants.

OCM, a modification of optical coherence tomography, has previously been used for medical and mammalian applications (Boppart et al., 1997a, 1997b, 1998a, 1998b, 1998c, 1999; Tearney et al., 1997; Fujimoto et al., 1998; Herrmann et al., 1998; Ripandelli et al., 1998; Baumal, 1999; Chauhan and Marshall, 1999; Parisi et al., 1999). Our system (Hoeling et al., 2000; Fig. 1) is similar to these systems, yet has notable advantages. First, our system simultaneously moves the focusing lens and reference mirror in a coordinated way to keep the lateral resolution constant throughout the depth of the sample. Second, our voxel data are spaced roughly uniformly in all three dimensions, so that our images have comparable resolution in all three dimensions. This uniform voxel density facilitates the rotation, cropping, and slicing of the images (Fig. 3; http://www.plantphysiol.org).

OCM is substantially different from other imaging technologies. It is advantageous in that it can penetrate to tissue depths approximately 10-fold greater than that of a confocal microscope (Running et al., 1995; Haseloff, 1999; Paddock, 1999). Some signal attenuation occurs with OCM with increasing scan depth, and can lead to shadows in the image. We are currently exploring techniques for correcting for this attenuation with depth. Imaging with a confocal microscope produces free radicals that are potentially damaging to living cells, which, along with photobleaching, typically limit confocal visualization to 1 to 2 h (Haseloff, 1999; Paddock, 1999). In contrast, OCM uses a low-intensity light source (300 μW) that produces no detectable damage. Similar imaging systems and intensities are used to scan living human retinas (Baumal, 1999; Chauhan and Marshall, 1999; Gurses-Ozden et al., 1999; Parisi et al., 1999). We have used OCM to follow development in multiple independent plants for over 1 week, collecting more than 100 images each from separate, individual plants, and have observed no detectable damage or developmental alterations (J. Hettinger, A. Reeves, R.L. Parsons, M.E. Williams, R.C. Haskell, D.C. Petersen, R. Wang, and J.I. Medford, unpublished data).

Our OCM system has a number of features that make it a particularly useful tool for biological study. First, it detects back-scattered photons from inherent features of the plant or plant cells (Fig. 6). These features do not deteriorate during the imaging process. Second, the high light-scattering property associated with cytoplasmically dense cells provides a type of natural endogenous developmental marker to follow over time. Third, OCM allows imaging of plants in situ, without removal from soil or growth media. Fourth, images are acquired rapidly. We currently acquire an image of the Arabidopsis shoot in 5.5 min, and improvements under way will reduce the collection time to approximately 1 min. Because of the rapid acquisition of images without cell or tissue damage, OCM allows us to obtain successive images of one plant at near real time to examine biological processes. Finally, our specific OCM system has been optimized for three-dimensional data collection and display. As shown in Figures 3 through 7, our data can be disassembled and viewed as cropped three-dimensional images or two-dimensional slices. The lower light-scattering values obtained for the blue boundary voxels are fortuitous in that they allow us to identify the outer surface of organs and/or tissue. OCM images resemble SEMs when viewed with a high α-parameter, which ren-

ders the voxels opaque (Figs. 2–4). By reducing the opacity of lower-value voxels including the boundary voxels, underlying light-scattering patterns can be seen (Fig. 5).

The biological basis of light scattering has been the focus of study (Dunn and Richards-Kotum, 1996; Drezek et al., 1999). Theoretical and experimental evidence suggest that certain inherent features of living cells are highly light scattering (Drezek et al., 1999). Specifically, cells with high nucleo-cytoplasmic ratios, cells that have large numbers of small organelles, and cells with folded membranes are highly light scattering. Our results are consistent with these studies. Figure 6 shows that nuclei are highly light scattering, the cytoplasm is intermediate in its light-scattering property, and the vacuole and cell wall are much less light scattering.

Within the Arabidopsis shoot apex, the light-scattering patterns are highly reproducible and are found in positions and at times consistent with biological function. The most highly scattering regions of the shoot apex have densely cytoplasmic cells with high nucleo-cytoplasmic ratios (Steeves and Sussex, 1989; Lyndon, 1990). For example, stipules are highly light scattering (Fig. 5). Although the function of Arabidopsis stipules is not known, they have large, prominent nuclei and nucleoli and are transcriptionally active (Steeves and Sussex, 1989; Medford et al., 1992). In developing leaf primordia, the distal-most tip of the leaf is most highly light scattering (Fig. 5). This region is known to retain cells that are densely cytoplasmic, at a time when more proximal leaf cells are expanding (Poethig and Sussex, 1985).

With OCM, the propagating light beam will first encounter surface regions such as the tip of leaf primordia. Therefore, a question arises as to whether the large signal in such regions is due to the highly scattering nature of the cells or to the large refractive index mismatch at the air-tissue interface. We tested this by imaging plants from above (standard imaging), then turning the plant to a horizontal position and imaging the same plant again. Light-scattering patterns such as those found in leaf primordia were qualitatively comparable. Furthermore, we routinely saw highly light-scattering regions such as the stipules and the apical meristem that were considerably below the air-tissue interface.

We also found a horseshoe-shaped pattern of intermediate light scattering in developing primordia (Figs. 3 and 5). This pattern is most apparent when images of leaf primordia are cropped (Fig. 3) or when a leaf primordium is isolated, viewed with reduced α, and rotated (Fig. 5; http://www.plantphysiol.org). This intermediate light-scattering pattern is consistent with regions in which the leaf blade is being specified (McHale, 1993; Tsuge et al., 1996). The shoot apical meristem was found to have an intermediate to high light-scattering pattern (Fig. 7). Our preliminary data suggest that the light-scatter pattern in meristems may be dynamic, changing as frequently as every 2 h.

A non-destructive in vivo imaging technology has been developed and used to image plants and plant cells. Imaging plants by OCM causes no apparent damage and provides information about inherent light-scattering properties of cells. Therefore, it provides a new technology with which to follow plant development and responses to exogenous factors.

MATERIALS AND METHODS

Plant Material

Arabidopsis plants were grown in a growth chamber (model AR-60L, Percival, Boone, IA) in soil (Sunshine Mix, Sun-Gro Horticulture, Bellevue, WA) at 23°C with a 16-h light/8-h dark cycle. All Arabidopsis plants were of the Columbia ecotype and in the *glabrous-1* (*gl-1*) genetic background. Within 5 min of OCM imaging, plants were fixed in FAA or 50% (v/v) ethanol. Following fixation, plants were embedded in LR White medium (Polysciences, Warrington, PA), and 1-μm sections were prepared and stained with 1% (w/v) toluidine blue, as previously described (Medford et al., 1992). Scanning electron micrographs were taken as described previously (Medford et al., 1992), except the critical point drying used a model E3100 (Bio-Rad, Hercules, CA), sputter coating used a Hummer VII (Anatech Ltd., Alexandria, VA), and SEM used a model 505 (Philips, Eindhoven, The Netherlands). Arabidopsis suspension-cultured cells were originally described by Davis and Ausubel (1989) and were the kind gift of Dr. Farida Safadi-Chamberlain (A.S.N. Reddy Laboratory, Colorado State University). Cells were maintained in the medium and conditions described by Davis and Ausubel (1989). Maize (*Zea mays* var. *rugosa*) (Carolina Biological Supply, Burlington, NC) plants were germinated in the growth chamber under the conditions described above. Images were collected from a leaf of a 14-d-old plant.

Construction and Operation of the Optical Coherence Microscope

Details of OCM can be found in Hoeling et al. (2000) and are shown schematically in Figure 1. Computer analysis of OCM data employs custom-designed AVS Express software (Advanced Visualization Systems, Waltham, MA) as described in Hoeling et al. (2000). Three-dimensional OCM data sets were generated by assigning a value to each voxel in the sample volume. Parallel rays traced through the three-dimensional data set were projected onto the two-dimensional viewing screen. All voxels in the volume along a ray contribute to the value of the corresponding pixel on the two-dimensional viewing screen. Because the ray does not always go through the center of a voxel, values at a given point along the ray can be computed by interpolating the values of the voxels in the vicinity of the ray (trilinear algorithm). Alternatively, the value of the nearest neighbor voxel can be used (point algorithm).

Another consideration when blending voxels along a ray is their opacity value. Small opacity values mean that many voxels will contribute to a pixel value. Therefore, the two-dimensional image generated with small opacity values will contain information about the interior of the three-dimensional data set as well as the surface voxels nearest the viewing screen. Larger opacity values will yield a two-dimensional image that is similar to a surface rendering of the data set. All plant images were collected from soil-grown plants under normal laboratory light and temperature conditions.

ACKNOWLEDGMENTS

The authors thank Dr. Scott Fraser for suggesting the use of OCM to examine plants. We acknowledge the work and assistance of numerous Harvey Mudd College undergraduates in supporting the OCM project. We thank Dr. Farida Sadi-Chamberlain in A.S.N. Reddy's laboratory for the kind gift of the Arabidopsis aneuploid cells. We thank Dr. David Marks for advice about trichomes and the *glabrous* mutant.

Received November 22, 1999; accepted February 8, 2000.

LITERATURE CITED

Barton MK, Poethig RS (1993) Formation of the shoot apical meristem in *Arabidopsis thaliana:* an analysis of development in the wild type and in the *shootmeristemless* mutant. Development **119:** 823–831

Baumal CR (1999) Clinical applications of optical coherence tomography. Curr Opin Ophthalmol **10:** 182–188

Boppart S, Brezinski M, Bouma B, Tearney G, Fujimoto J (1997a) Investigation of developing embryonic morphology using optical coherence tomography. Dev Biol **177:** 54–63

Boppart S, Tearney G, Bouma B, Southern J, Brezinski M, Fujimoto J (1997b) Noninvasive assessment of the developing *Xenopus* cardiovascular system using optical coherence tomography. Proc Natl Acad Sci USA **94:** 4256–4261

Boppart SA, Bouma BE, Pitris C, Southern JF, Brezinski ME, Fujimoto JG (1998a) In vivo cellular optical coherence tomography imaging. Nat Med **4:** 861–865

Boppart SA, Bouma BE, Pitris C, Tearney GJ, Southern JF, Brezinski ME, Fujimoto JG (1998b) Intraoperative assessment of microsurgery with three-dimensional optical coherence tomography. Radiology **208:** 81–86

Boppart SA, Brezinski ME, Pitris C, Fujimoto JG (1998c) Optical coherence tomography for neurosurgical imaging of human intracortical melanoma. Neurosurgery **43:** 834–841

Boppart SA, Herrmann J, Pitris C, Stamper DL, Brezinski ME, Fujimoto JG (1999) High-resolution optical coherence tomography-guided laser ablation of surgical tissue. J Surg Res **82:** 275–284

Chauhan DS, Marshall J (1999) The interpretation of optical coherence tomography images of the retina. Investig Ophthalmol Vis Sci **40:** 2332–2342

Davis KR, Ausubel FM (1989) Characterization of elicitor-induced defense responses in suspension-cultured cells of *Arabidopsis*. Mol Plant-Microbe Interact **2:** 363–368

Dolan L, Janmaat K, Willemsen V, Linstead P, Poethig S, Roberts K, Scheres B (1993) Cellular organisation of the *Arabidopsis thaliana* root. Development **119:** 71–84

Drezek R, Dunn A, Richards-Kortum R (1999) Light scattering from cells: finite-difference time-domain simulations and goniometric measurements. Appl Optics **38:** 3651–3661

Dunn A, Richards-Kotum R (1996) Three-dimensional computation of light scattering from cells. IEEE J Sel Topics Quantum Electron **2:** 898–905

Faust M, Wang PC, Maas J (1997) The use of magnetic resonance imaging in plant science. Hortic Rev **20:** 225–266

Fercher AF (1996) Optical coherence tomography. J Biomed Optics **1:** 157–173

Fujimoto JG, Bouma B, Tearney GJ, Boppart SA, Pitris C, Southern JF, Brezinski ME (1998) New technology for high-speed and high-resolution optical coherence tomography. Ann NY Acad Sci **838:** 95–107

Gausman HW (1977) Reflectance of leaf components: remote sensing of environment. Remote Sens Environ **6:** 1–9

Gilbert SF (1998) Development Biology, Ed 5. Sinauer Associates, Sunderland, MA

Gurses-Ozden R, Ishikawa H, Hoh ST, Liebmann JM, Mistlberger A, Greenfield DS, Dou HL, Ritch R (1999) Increasing sampling density improves reproducibility of optical coherence tomography measurements. J Glaucoma **8:** 238–241

Haseloff J (1999) GFP variants for multispectral imaging of living cells. Methods Cell Biol **58:** 139–151

Herrmann JM, Brezinski ME, Bouma BE, Boppart SA, Pitris C, Southern JF, Fujimoto JG (1998) Two- and three-dimensional high-resolution imaging of the human oviduct with optical coherence tomography. Fertil Steril **70:** 155–158

Hoeling BM, Fernandez AD, Haskell RC, Myers WR, Petersen DC, Ungersma SE, Wang R, Williams ME (2000) An optical coherence microscope for three-dimensional imaging in developmental biology. Optics Express **6:** 136–147

Izatt JA, Kulkarni MD, Wang H-W, Kobayashi K, Sivak MV Jr (1996) Optical coherence tomography and microscopy in gastrointestinal tissues. IEEE J Sel Topics Quantum Electron **2:** 1017–1028

Long JA, Moan EI, Medford JI, Barton MK (1996) A member of the KNOTTED class of homeodomain proteins encoded by the *STM* gene of *Arabidopsis*. Nature **379:** 66–69

Lyndon RF (1990) The Cellular Basis. *In* M Black, J Chapman, eds, Plant Development. Unwin Hyman, Winchester, MA

Masters BR (1999) Early development of optical low-coherence reflectometry and some recent biomedical applications. J Biomed Optics **4:** 236–247

McHale NA (1993) *LAM-1* and *FAT* genes control development of the leaf blade in *Nicotiana sylvestris*. Plant Cell **5:** 1029–1038

Medford JI, Behringer FJ, Callos JD, Feldmann KA (1992) Normal and abnormal development in the *Arabidopsis* vegetative shoot apex. Plant Cell **4:** 631–643

Paddock SW (1999) Confocal laser scanning microscopy. Biotechniques **27:** 992–1004

Parisi V, Manni G, Spadaro M, Colacino G, Restuccia R, Marchi S, Bucci MG, Pierelli F (1999) Correlation between morphological and functional retinal impairment in multiple sclerosis patients. Investig Ophthalmol Vis Sci **40:** 2520–2527

Poethig RS, Sussex IM (1985) The cellular parameters of leaf development in tobacco: a clonal analysis. Planta **165:** 170–184

Ripandelli G, Coppe AM, Capaldo A, Stirpe M (1998) Optical coherence tomography. Semin Ophthalmol **13:** 199–202

Running MP, Clark SE, Meyerowitz EM (1995) Confocal microscopy of the shoot apex. Methods Cell Biol **49:** 217–229

Steeves TA, Sussex IM (1989) Patterns in Plant Development, Ed 2. Cambridge University Press, New York

Tearney GJ, Brezinski ME, Bouma BE, Boppart SA, Pitris C, Southern JF, Fujimoto JG (1997) *In vivo* endoscopic optical biopsy with optical coherence tomography. Science **276:** 2037–2039

Tsuge T, Tsukaya H, Uchimiya H (1996) Two independent and polarized processes of cell elongation regulate leaf blade expansion in *Arabidopsis thaliana* (L.) Heynh. Development **122:** 1589–1600

van den Berg C, Willemsen V, Hage W, Weisbeek P, Scheres B (1997a) Cell fate in the Arabidopsis root meristem determined by directional signaling. Nature **378:** 62–65

van den Berg C, Willemsen V, Hendriks G, Weisbeek P, Scheres B (1997b) Short-range control of cell differentiation in the *Arabidopsis* root meristem. Nature **390:** 287–289